



Micromechanical characterisation of TRIP-assisted multiphase steels by in situ neutron diffraction

Journal:	<i>Philosophical Magazine & Philosophical Magazine Letters</i>
Manuscript ID:	TPHM-05-Aug-0363.R1
Journal Selection:	Philosophical Magazine
Date Submitted by the Author:	08-Dec-2005
Complete List of Authors:	Jacques, Pascal; Universite catholique de Louvain, IMAP Furnemont, Quentin; Universite catholique de Louvain, IMAP Godet, Stephane; Universite catholique de Louvain, IMAP Pardoen, Thomas; Universite catholique de Louvain, IMAP Conlon, Kelly; Atomic Energy of Canada Ltd., Chalk River Laboratories Delannay, Francis; Universite catholique de Louvain, IMAP
Keywords:	steel, neutron diffraction, micromechanics, martensitic transformations
Keywords (user supplied):	TRIP effect, flow properties



1 **Micromechanical characterisation of TRIP-assisted multiphase steels by *in situ***
2
3 **neutron diffraction**
4
5
6

7 P.J. JACQUES^{**†}, Q. FURNEMONT[†], S. GODET[†], T. PARDOEN[†], K.T. CONLON[‡], F. DELANNAY[†]
8
9

10
11 [†] Université catholique de Louvain, Département des Sciences des Matériaux et des Procédés,
12
13 IMAP, Place Sainte Barbe 2, B-1348 Louvain-la-Neuve, Belgium
14

15 [‡] Atomic Energy of Canada Ltd., Chalk River Laboratories, Chalk River, Ontario, K0J 1P0, Canada
16
17
18
19
20

21 **Abstract**
22
23
24

25 The flow behaviour of the constitutive phases in multiphase steels possibly exhibiting a
26 mechanically-induced phase transformation (TRIP effect) is investigated using neutron
27 diffraction conducted during uniaxial tensile loading. The BCC and FCC lattice strains
28 of several specimens containing different amounts ferrite, bainite, martensite and
29 metastable retained austenite are measured along elastic and plastic deformation. The
30 validity of the measurements as well as the strengthening resulting from the TRIP effect
31 are evaluated on the basis of overall mechanical equilibrium.
32
33
34
35
36
37
38
39

40 *Keywords:* neutron diffraction; multiphase steels; flow properties; TRIP effect
41
42

43
44 **1. Introduction**
45
46
47

48 The mechanical properties of the phases present in Fe and Fe-C based alloys can vary in a wide
49 range, from the soft and ductile ferrite to the ultra high strength martensite. The design of new steel
50
51
52
53
54
55
56
57
58
59
60

1 grades and complex microstructures combining these phases like *in situ* composites is prompted by
2 the search for new high performance structural steels adapted for demanding applications in the
3 automotive industry. After the Dual Phase (ferrite – martensite) steels in the 1970s, the 1990s have
4 seen the development of the so-called *TRIP-assisted multiphase steels* [1 - 4]. These steels present
5 multiphase microstructures consisting of an intercritical ferrite matrix and a dispersion of
6 multiphase grains of bainite, martensite, and metastable retained austenite that can transform during
7 straining. The TRIP effect, i.e. the mechanically-activated martensitic transformation, known for
8 quite a long time in highly alloyed austenitic and martensitic steels [5 - 7], has regained a large
9 interest with these low alloy steels. Indeed, in addition to common strengthening mechanisms such
10 as grain refinement, precipitation or composite strengthening, both strength and formability can be
11 improved by the capacity of the martensitic transformation. In the case of the present multiphase
12 steels, the (meta)stabilisation of austenite at room temperature is ensured by increasing its carbon
13 content through specifically designed thermal or thermomechanical treatments [1, 8].
14
15
16
17
18
19
20
21
22
23
24
25
26
27

28 Thanks to their increased work hardening rate, TRIP-assisted multiphase steels present large
29 uniform elongations and high strength levels. A complete picture of the microscopic mechanisms
30 involved in enhancing the work hardening capability has not fully emerged yet. Numerous studies
31 have dealt with the relationship between the processing parameters, the genesis of multiphase
32 microstructures, the austenite retention, and the resulting properties during straining [2, 3].
33 However, little has been reported on the microscopic plastic behaviour of these steels [1, 3, 9, 10].
34 Nevertheless, two strengthening mechanisms definitely play a role in TRIP-aided steels: (i) the
35 composite-like strengthening of the microstructure, which continuously evolves during straining as
36 a result of the mechanically-activated austenite transformation and, (ii) the extra strain hardening
37 induced by the plastic flow associated to the transformation strain. Furthermore, TRIP-assisted
38 multiphase steels present the unique feature that the TRIP effect occurs in small austenite grains
39
40
41
42
43
44
45
46
47
48
49
50
51
52
53
54
55
56
57
58
59
60

1 dispersed in a soft ferritic matrix. Accommodation of the transformation strain thus leads to a
2
3 dislocation strengthening of the surrounding ferrite grains. [9].

Deleted: so that interactions can also arise between these two sources can also play a role through dislocation strengthening

4
5
6
7 In order to develop a micromechanical model for predicting the flow behaviour of composite
8 materials such as TRIP-aided steels, it is essential to know the flow properties of each constitutive
9 phase. The determination of these flow properties is quite challenging since it can be quite tricky to
10 process the same phases as mono-phase materials. For instance, in TRIP-aided steels, the austenite
11 is retained at room temperature not only thanks to high C enrichments (up to 1.2 wt.%) but also
12 thanks to grain refinement (down to about 1 μ m) that cannot be obtained by hot rolling. The
13 elastoplastic behaviour of each phase must thus be measured *in situ*.
14
15
16
17
18
19

20
21
22 Once the flow properties have been measured, the interactions between the constitutive
23 phases can then be investigated. Indeed, stress and strain partitioning arises at the scale of the
24 microstructure due to the different mechanical behaviours of the phases. Beyond the simple upper
25 and lower bounds given by the Voigt and Reuss assumptions, a realistic micromechanical modelling
26 of composite microstructures requires the elucidation of the mesoscopic interactions between the
27 phases. Moreover, TRIP-aided steels constitute 'evolving composites' since the proportions of
28 austenite and martensite continuously change during straining, which modifies the stress
29 partitioning.
30
31
32
33
34
35
36
37
38
39

40 Neutron diffraction is well adapted for the measurement of phase-specific or grain
41 orientation-specific stresses in multiphase materials due to its selectivity based on the crystal
42 lattices and to the large size of the gauge volume [11]. Stress measurement by means of diffraction
43 is essentially a measurement of microscopic strains, i.e. the comparison of the stress-free lattice
44 spacing of a given crystallographic plane (or the mean lattice parameter of a given phase) with the
45 lattice spacing of the loaded specimen. Several studies have demonstrated the possibility of
46
47
48
49
50

1 monitoring the stress partitioning operating between the constitutive phases of various materials
2
3 (Fe-Cu [11], ferrite –cementite [12, 13], duplex steels [14], Be – Al composites [15]) or between
4
5 differently oriented crystallites of single phase materials (Ti, Fe Al, Cu, ... [12, 13, 16, 17, 18])
6
7 thanks to *in situ* neutron diffraction during mechanical straining. Some studies were also devoted to
8
9 the mechanically-induced martensitic transformation either in shape memory alloys [19, 20] or in
10
11 low alloy TRIP-aided steels [21].
12

13
14 The purpose of this study is to contribute to a better understanding of the factors governing
15
16 the elastoplastic behaviour of multiphase steels possibly exhibiting a TRIP effect. Particularly,
17
18 thanks to *in situ* neutron diffraction during uniaxial straining, the stress partitioning between ferrite,
19
20 bainite, austenite and martensite could be determined. Furthermore, the strengthening resulting from
21
22 the TRIP effect has also been analysed.
23
24
25
26
27

28 **2. Materials and Experimental Procedures**

31 **2.1. Materials**

32
33
34
35 **2.1.1. Chemical compositions and thermomechanical processing.** Two steel grades differing by
36
37 their carbon contents were investigated in this study. Their chemical compositions are given in
38
39 Table I together with their respective denomination (03C and 04C) referring to their C contents.
40
41 Cast ingots of these grades were processed in such a way as to generate several multiphase
42
43 microstructures. Cold rolled and annealed Dual Phase and TRIP-assisted multiphase steels were
44
45 processed from steel 03C while steel 04C was hot rolled and processed into a bainite/austenite
46
47 microstructure. More details about the processing procedures can be found in [2, 22].
48
49
50
51
52
53
54
55
56
57
58
59
60

1 [Insert Table I about here]
2
3
4

5 **2.1.2. Microstructures and uniaxial flow properties.** Four typical microstructures corresponding
6 to either stable or metastable multiphase microstructures were investigated in this study. Figure 1
7 presents the general morphology of these microstructures. Specimens DP, TRIP1 and TRIP2 were
8 processed from steel 03C while specimen B was processed from steel 04C. Specimen DP (Figure
9 1a) was directly quenched after intercritical annealing so that it presents a Dual Phase ferrite-
10 martensite microstructure. Specimens TRIP1 and TRIP2 (Figure 1b and 1c) present multiphase
11 microstructures consisting of ferrite, bainite and retained austenite. They differ by the bainitic
12 holding conditions and consequently by the volume fraction and carbon content of the retained
13 austenite. Finally, specimen B (Figure 1d) exhibits a hot rolled bainite/austenite microstructure.
14
15
16
17
18
19
20
21

22 [Insert Figure 1 about here]
23
24
25
26
27

28 The volume fractions of the constitutive phases have been quantitatively determined for
29 each specimen by combining techniques such as image analysis, dilatometry and Mössbauer
30 spectroscopy or X-ray diffraction. These two last techniques have also been used to measure the
31 amount of remaining austenite in specimens strained to increasing levels. Table II summarises the
32 initial volume fractions for the different specimens and gives the retained austenite carbon content
33 estimated by Mössbauer spectroscopy. While specimen DP presents a 50-50 ferrite-martensite
34 microstructure, specimens TRIP1 and TRIP2 differ by the amount of bainite and retained austenite
35 [2, 23]. Specimen B contains a large amount of retained austenite together with bainite [22].
36
37
38
39
40
41
42
43
44

45 [Insert Table II about here]
46
47
48
49
50
51
52
53
54
55
56
57
58
59
60

1 As shown in Figure 2a , each specimen exhibits a particular combination of strength and
2 elongation during uniaxial tensile tests. Specimen DP presents a very high strength with a uniform
3 elongation limited to less than 0.05. Specimens TRIP1 and B exhibit the best combinations of
4 strength and uniform elongation while the strength and uniform elongation of specimen TRIP2 are
5 smaller. As already shown elsewhere [9], these different combinations of strength and uniform
6 elongation result from different work-hardening behaviours during plastic straining as demonstrated
7 by the evolution with strain of the incremental work-hardening exponent ($n_{incr} = d\ln(\sigma)/d\ln(\epsilon)$)
8 given in Figure 2b. Specimens TRIP1 and B present better combinations of properties due to a high
9 and/or increase of the work-hardening for a wider range of plastic strain.

10
11
12
13
14
15
16
17
18
19
20 [Insert Figure 2 about here]
21
22
23

24 The austenite transformation rates in specimens TRIP1, TRIP2 and B are given in Figure 3.
25 Specimen B, which contains the largest amount of retained austenite, also presents the largest
26 transformation rate. Specimen TRIP1 presents a slightly lower transformation rate than specimen B.
27 In contrast, specimen TRIP2 exhibits almost no austenite transformation during straining due to a
28 higher carbon enrichment during the bainite transformation. From this result, it can be concluded
29 that the flow properties under uniaxial tension exhibited by the different specimens result not only
30 from the mechanical properties of the constitutive phases but also from the possible occurrence of
31 the TRIP effect. In the following, the role of the TRIP effect on the phase stresses will be
32 highlighted by comparing specimens DP and TRIP2, which exhibit no (or hardly any) TRIP effect
33 with specimens TRIP1 and B.

Deleted: phases

34
35
36
37
38
39
40
41
42
43
44
45 [Insert Figure 3 about here]
46
47
48
49
50
51
52
53
54
55
56
57
58
59
60

1 **2.1.3. Texture.** As explained hereafter, the $\{211\}_\alpha$ and $\{311\}_\gamma$ reflections have been chosen for the
2
3 determination by neutron diffraction of the stress level of the BCC and FCC phases, respectively. In
4
5 order to ensure the representativity of the collected data and suitable conditions of measurements
6
7 (i.e. avoiding the disappearance of the diffraction peaks during straining), it was necessary to check
8
9 the texture level of the different specimens and its evolution during straining. Figure 4 presents the
10
11 $\{211\}_\alpha$ and $\{311\}_\gamma$ pole figures (recalculated from the ODF), both before straining and after
12
13 uniform elongation in the case of specimen TRIP1 that presents the strongest texture among the
14
15 different specimens. This Figure demonstrates that the specimens are only weakly textured and that
16
17 the degree of texturing does not increase much during straining.

18
19
20 [Insert Figure 4 about here]
21
22

23 24 **2.2. Experimental Procedure**

25
26
27
28 **2.2.1. Stress rig set up.** Tensile testing coupled with neutron diffraction was conducted at the NRC
29
30 labs of AECL, Chalk River, Canada using a specifically adapted screw-driven tensile testing rig
31
32 mounted on the L3 diffractometer. Elastic strains in the phases were obtained by measuring the
33
34 change of lattice spacing d of specific diffraction peaks using a nominal monochromatic incident
35
36 neutron wavelength of 1.5 Angströms reflected from a Ge single crystal. $\{211\}$ and $\{311\}$
37
38 reflections were chosen for the BCC and FCC lattices, respectively. Indeed, these two particular
39
40 planes have been shown to present a linear response with the applied stress, meaning that they are
41
42 quite insensitive to the intergranular strains. They thus closely represent the macroscopic stress
43
44 behaviour of FCC and BCC lattices [12, 16, 24, 25]. All specimens were tested in the 'Young
45
46 configuration', i.e. with the diffraction vector parallel to the tensile axis. Some specimens were also
47
48 tested in the 'Poisson configuration', i.e. with the diffraction vector perpendicular to the tensile axis.

49
50 Figure 5 illustrates the geometry of both configurations. Data were collected in the form of raw

Deleted: Data's

neutron counts versus scattering angle by rocking an 8-element position sensitive detector (angular width $\sim 0.6^\circ$) over the Bragg peaks in 0.1° steps in 2θ . During the measurements, the stress-rig was continuously half-angled in a “ $\theta - 2\theta$ ” geometry to maintain the scattering vector parallel or perpendicular to the tensile axis of the specimen. Counting times for collecting Bragg peaks ranged from 5 minutes for $\{211\}_\alpha$, to 20 minutes to 2 hours for $\{311\}_\gamma$, depending on the remaining austenite volume fraction. The signal to noise ratio was always kept larger than 3. The incident and the scattered neutron beams were collimated with Cd coated steel “soller” slits such that the nominal horizontal angular divergence was approximately 0.5° . Load or displacement control was applied during the measurement stages while between these stages, straining was carried out at a constant crosshead displacement of 1 cm/minute.

[Insert Figure 5 about here]

The elastic lattice strain in the phases was computed as

$$\varepsilon_{hkl} = \frac{d^{hkl} - d_0^{hkl}}{d_0^{hkl}} \quad (1)$$

where d_0^{hkl} is the initial stress-free d -spacing of the (hkl) planes and d^{hkl} is the instantaneous d -spacing under loading. The d -spacings were calculated by fitting the collected peaks by Gaussian line-shapes. The initial residual stress level was also estimated in the different specimens by measuring the diffracted peaks in different directions with respect to the specimens (i.e. rolling, transverse and normal directions). The residual stresses in the phases of the different specimens were found to be always very small (10 to 30 MPa) and of the order of the resolution of the diffraction measurements.

A particular peak deconvolution procedure was applied in the case of specimen DP. Indeed, martensite presents a body-centred tetragonal (BCT) structure with a tetragonality that depends on

1 its carbon content ($c/a \approx 1.04$ in the present case). This tetragonality causes the split of some
2
3 diffraction peaks into doublets. There is thus an overlap of the $\{211\}_{\alpha'}$ and $\{112\}_{\alpha'}$ martensite
4
5 peaks and of the $\{211\}_{\alpha}$ diffraction peak of ferrite in specimen DP. Figure 6 shows the resulting
6
7 shape of the $\{211\}_{\alpha}$, $\{211\}_{\alpha'}$ and $\{112\}_{\alpha'}$ peaks. Consequently, the positions of the martensitic
8
9 peaks were very difficult to define. In order to calibrate the deconvolution procedure of these peaks
10
11 in specimen DP without arbitrary assumptions about the shape of the martensite doublet, diffraction
12
13 experiments were also conducted on a fully martensitic specimen. This specimen presented the
14
15 same C content as the martensite of specimen DP. Furthermore, the heat treatment applied to this
16
17 steel grade involved several fast heating and cooling cycles between room temperature and 800°C
18
19 in order to refine the grains down to a size comparable to the martensite grain size of specimen DP.
20
21 The peak fitting procedure consisted in determining the peak width on this monophasic specimen
22
23 while imposing physical constraints for the other peak parameters. The estimated peak broadening
24
25 was then imposed for the martensite peak fitting in specimen DP. Figure 6 exemplifies the resulting
26
27 deconvoluted peaks.

Deleted: its processing

Deleted:

Deleted: Diffraction measurements on this specimen allowed to calibrate the fitting parameters for the martensite.

28
29
30 [Insert Figure 6 about here]

31
32
33
34 It is worth mentioning that it was impossible to measure the lattice strain of martensite for
35
36 the other specimens. Indeed, the maximum martensite amount in specimens TRIP1 or B was of the
37
38 order of 10 to 15%, which is too small with respect to the background level. However, this
39
40 martensite doublet did not influence the $\{211\}_{\alpha}$ peak fitting in these specimens.

41 42 43 3. Results

44
45
46
47
48 Figure 7a presents the evolution of the lattice strain in the loading direction (calculated by (1)) for
49
50 the $\{211\}_{\alpha}$ and $\{211\}_{\alpha'}$ reflections as a function of the macroscopic strain during tensile straining of
51

1 specimen DP. As it could be anticipated, the two curves show that the lattice strain, and thus the
2 stress level, is much larger in martensite than in ferrite. Furthermore, while the lattice strain of
3 $\{211\}_\alpha$ seems to rapidly saturate during straining, the lattice strain of $\{211\}_\alpha'$ keeps increasing quite
4 monotonously.
5
6
7

8
9
10 [Insert Figure 7 about here]
11
12

13
14 Figure 7b shows the evolutions of the lattice strain in the tensile direction as a function of
15 the macroscopic strain for the BCC (ferrite + bainitic ferrite) and FCC (austenite) phases of
16 specimen TRIP1. After a linear increase with the macroscopic strain, the lattice strain of both
17 phases present sharp changes of slope at different levels. The lattice strain measured from the
18 $\{311\}_\gamma$ reflection is larger than for $\{211\}_\alpha$, indicating that the stress level is larger in the austenite
19 than in the ferrite/bainite mixture. It is also worth noting that the accuracy of the measurements for
20 the FCC phase remains quite good at large plastic strain even though the amount of retained
21 austenite has much decreased (Figure 3).
22
23
24
25
26
27
28
29

30
31 A similar evolution of the lattice strain of $\{211\}_\alpha$ and $\{311\}_\gamma$ in the tensile direction is
32 depicted in Figure 7c for specimen TRIP2. The austenite is also more loaded than the ferritic
33 phases. Furthermore, the lattice strains of BCC and (especially) FCC are larger in specimen TRIP2
34 than in specimen TRIP1.
35
36
37
38
39
40

41
42 The lattice strain in the tensile direction vs. the macroscopic true strain is given in Figure 7d
43 for specimen B. In this specimen, the BCC phase consists only of bainitic ferrite (while it consisted
44 mainly of intercritical ferrite in specimens TRIP1 and TRIP2). Even though the change of slope and
45 the global level of lattice strain for the $\{211\}_\alpha$ peak is larger in specimen B than in specimens
46 TRIP1 and TRIP2, the austenite is still the strongest phase.
47
48
49
50
51

1
2
3 Finally, the transverse lattice strains of both BCC and FCC phases measured during
4 straining of specimens TRIP1 and TRIP2 are shown in Figure 8. The transverse values are also
5 larger for the austenite in both specimens.
6
7

8
9
10 [Insert Figure 8 about here]
11

12 13 14 **4. Discussion**

15
16
17 In order to convert the measured lattice strains into the stress levels prevailing within the different
18 phases, it is first necessary to estimate the diffraction elastic moduli E^{hkl} and ν^{hkl} . These moduli can
19 be calculated using the single crystal elastic constants while assuming a particular stress partitioning
20 (Voigt, Reuss, Hill, Kröner) between the grains oriented in different directions. It is worth noting
21 that no texture effect is accounted for by these assumptions. These moduli can also be estimated by
22 considering, in the elastic regime, the evolution of the longitudinal lattice strain with the
23 macroscopic stress (for the Young modulus) and the ratio of the longitudinal and transverse lattice
24 strains (for the Poisson ratio). This method implicitly assumes Reuss and Voigt partitioning for the
25 Young modulus and Poisson ratio, respectively. Table III summarises the values calculated and
26 derived from the experiments for both E^{hkl} and ν^{hkl} for the different specimens. For the calculated
27 moduli, the Kröner assumption was considered using the crystal elastic constants taken from [12,
28 13, 17] for the BCC and FCC iron.
29
30
31
32
33
34
35
36
37
38
39
40
41
42

43 [Insert Table III about here]
44
45

46
47 Table III demonstrates a very good agreement between the measured and calculated elastic
48 moduli. As shown previously [12, 16, 24, 25], the chosen reflections for both the BCC and FCC
49
50

lattices are quite insensitive to the intergranular strains and closely represent the mean stress behaviour of both lattices. As a consequence, the different assumptions for the stress partitioning give quite similar results. Furthermore, ferrite and austenite in steels present quite similar crystallographic elastic constants so that elastic partitioning effects will be small.

Using the measured E^{hkl} and ν^{hkl} given in Table III, the stress level in the different phases were inferred from the measured lattice strain. Due to the geometry of the tensile test which involves $\varepsilon_{22} = \varepsilon_{33}$ (with ε_{11} along the tensile axis), two lattice strain components are sufficient to determine the mean stress level in each phase using

$$\bar{\sigma}_{11} = \frac{E^{hkl}}{(1 + \nu^{hkl})(1 - 2\nu^{hkl})} \left\{ (1 - \nu^{hkl}) \varepsilon_{11}^{hkl} + 2 \nu^{hkl} \varepsilon_{22}^{hkl} \right\} \quad (2a)$$

$$\bar{\sigma}_{22} = \frac{E^{hkl}}{(1 + \nu^{hkl})(1 - 2\nu^{hkl})} \left\{ \varepsilon_{22}^{hkl} + \nu^{hkl} \varepsilon_{11}^{hkl} \right\} \quad (2b)$$

When the transverse strain was not available, the mean stress level was estimated using

$$\bar{\sigma}_{11} = E^{hkl} \varepsilon_{11}^{hkl} \quad (3)$$

The importance of the transverse stress and the validity of Eq. (3) can be assessed on Figures 9a and 9b which compare the evolutions with the macroscopic true strain of $\bar{\sigma}_{11}$ calculated using equations (2a) or (3) for specimens TRIP1 and TRIP2, respectively. These Figures demonstrate that the error brought about by neglecting the transverse lattice strain is quite small. As shown by the error bars drawn on these graphs, the difference is of the order of the experimental scattering, i.e. 50 – 60 MPa for both the BCC and FCC phases. Figure 10 presents the evolution of $\bar{\sigma}_{22}^{\alpha}$ and $\bar{\sigma}_{22}^{\gamma}$ with the macroscopic true strain for specimen TRIP2 (which exhibits almost no austenite transformation). Although both lattice strains of $\{211\}_{\alpha}$ and $\{311\}_{\gamma}$ were negative, the calculated stresses present opposite signs, ensuring the load equilibrium. Furthermore, the transverse stresses are quite small, particularly for the BCC phase. Finally, these results show that we are entitled to

Deleted: were

Deleted: calculate

1 | estimate the mean longitudinal phase stresses in specimens B and DP, even though the transverse
2 |
3 | lattice strains are unknown. The curves calculated using equations (3) are given in Figures 11 for
4 |
5 | these two specimens.
6 |
7 |

8 |
9 | [Insert Figure 9 about here]

10 | [Insert Figure 10 about here]

11 | [Insert Figure 11 about here]
12 |
13 |

14 |
15 |
16 | The measured lattice strain evolutions allow the estimation of the yield strength of the
17 | different phases. Indeed, a shift from the linear evolution of the lattice strain with respect to the
18 | macroscopic stress or strain corresponds to a change in the stress transfer between the phases and
19 | thus to the occurrence of a different deformation mechanism. The evolution of the macroscopic true
20 | stress as a function of the lattice strain is presented in Figure 12 for specimens TRIP2 and DP. At
21 | the point located by 'I', the BCC phase starts to yield, i.e. this phase is no more able to sustain a
22 | linear increase of stress for an imposed increase of load. Simultaneously, the FCC or BCT phase has
23 | to hold a larger stress as shown by the larger increase of their lattice strains with respect to the
24 | macroscopic stress. In specimen DP (Figure 12b), no other change of slope seems to occur for the
25 | lattice strain curve of $\{211\}_{\alpha'}$, suggesting that the martensite remains elastic up to the onset of
26 | necking. In specimen TRIP2, another change of slope, denoted 'II' on Figure 12a, corresponds to
27 | the yielding of the FCC phase. As pointed out by Figure 13, point II in this specimen is well related
28 | to the austenite yielding and does not correspond to the end of the Lüders plateau.
29 |
30 |
31 |
32 |
33 |
34 |
35 |
36 |
37 |
38 |
39 |
40 |
41 |

Deleted: allows

Deleted: to estimate

42 |
43 | [Insert Figure 12 about here]

44 | [Insert Figure 13 about here]
45 |
46 |
47 |
48 |
49 |
50 |
51 |
52 |
53 |
54 |
55 |
56 |
57 |
58 |
59 |
60 |

1 Table IV presents the yield strength measured for the different phases in each specimen and
2 converted using the corresponding elastic constants. It is quite remarkable that the austenite is
3 always the strongest phase. This result confirms previous measurements by nano-indentation [26] or
4 neutron diffraction [21]. It was not anticipated when considering the data published on highly-
5 alloyed fully austenitic TRIP steels (such data were sometimes used in the literature for the
6 modelling of the mechanical properties of the present Fe-C TRIP-aided steels [27, 28]). The present
7 austenite high yield strength is related to its high carbon content. Figure 14 presents the evolution of
8 the austenite yield strength as a function of its carbon content for the specimens investigated in this
9 paper as well as for some other specimens [23]. An increase of the order of 650 MPa per weight
10 percent of carbon is derived from these results. This strengthening rate is quite larger than the
11 strengthening effect reported for carbon in highly alloyed Ni-Cr austenitic steels [29, 30].
12
13
14
15
16
17
18
19
20
21
22
23

24 [Insert Table IV about here]

25 [Insert Figure 14 about here]

26
27
28
29
30 Results for another bainite – austenite specimen also processed from steel 04C (denoted B*)
31 has been added in Table IV and Figure 14. Both specimens B and B* differ by the hot rolling
32 schedule applied to the austenite prior to the bainitic holding [22]. As a consequence, austenite is
33 recrystallised in specimen B* while it is not in specimen B. Figure 14 shows that the austenite yield
34 strength is much higher in specimen B than in specimen B*. However, Table IV shows that the
35 hardening is not as large for the bainitic phase.
36
37
38
39
40
41
42

Deleted: also

Deleted: in specimens B and B*

43 As already pointed out, it seems that the martensite in specimen DP remains elastic up to the onset
44 of necking. The stress level at necking shown in Figure 12b (~2200MPa) corresponds to values
45 reported for martensite yielding or fracture [31].
46
47
48
49
50
51
52
53
54
55
56
57
58
59
60

The strength of the other phases can also be more precisely estimated by considering the mechanical equilibrium, which states that the applied stress is distributed among the different phases in relationship with their volume fractions and writes

$$\sigma(\varepsilon) = f_{\alpha} \sigma_{\alpha}(\varepsilon) + f_{\alpha_b}(\varepsilon) \sigma_{\alpha_b}(\varepsilon) + f_{\gamma}(\varepsilon) \sigma_{\gamma}(\varepsilon) + f_{\alpha'}(\varepsilon) \sigma_{\alpha'}(\varepsilon) \quad (4)$$

where f_i and σ_i refer to the volume fractions and average stresses of the different phases. This equation allows the assessment of the validity of the measurements. Equilibrium can first be applied to more precisely estimate the bainite yield strength. Indeed, the results of Table IV show that the yield strength of the BCC phase is quite different depending on the specimen that is considered. Actually, depending on the heat-treatment parameters, the so-called BCC phase corresponds to different amounts of intercritical ferrite and bainite, ranging from fully ferritic in specimen DP to fully bainitic in specimens B and B*. For the sake of comparison, a steel grade of composition 0.01C-1.5Mn-1.5Si was processed in the same conditions as for specimens TRIP1 and TRIP2. However, due to its very low C content, this steel grade presented a fully ferritic microstructure. Uniaxial tensile tests carried out on these fully ferritic specimens brought about the same yield strength of 520 MPa, independently of the processing parameters. This value is smaller than the stress at yielding of the BCC phases in specimens TRIP1 and TRIP2. Indeed, the BCC phases in these specimens consist not only of intercritical ferrite but also of bainite (which is not present in the fully ferritic specimens). Considering the mechanical equilibrium for the BCC phases, $\sigma_{BCC} = f_{\alpha} \sigma_{\alpha} + f_{\alpha_b} \sigma_{\alpha_b}$, the stress level of the bainitic phase just after the onset of yielding can be calculated for both specimens. Values of 840 MPa and 1240 MPa are found for bainite in specimens TRIP1 and TRIP2, respectively. These values agree perfectly with the estimated yield strength of bainite in specimens B and B* (bainitically transformed at a temperature quite similar to specimen TRIP1) and with previous results demonstrating the strengthening effect of a lower bainite transformation temperature [32].

Deleted: to assess

Figure 15 compares the macroscopic stress and the longitudinal or transverse stress recalculated from the measured lattice strains for the specimens in which there is (almost) no strain-induced phase transformation, i.e. specimens DP and TRIP2. The equilibrium writes in that cases $\sigma = f_{\alpha} \sigma_{\alpha} + f_{\alpha'} \sigma_{\alpha'}$ for specimen DP and $\bar{\sigma}_{11} = f_{BCC} \bar{\sigma}_{11}^{BCC} + f_{FCC} \bar{\sigma}_{11}^{FCC}$ or $\bar{\sigma}_{22} = f_{BCC} \bar{\sigma}_{22}^{BCC} + f_{FCC} \bar{\sigma}_{22}^{FCC}$ for specimen TRIP2, respectively. Figure 15 shows that, considering the experimental scattering, the recalculated stresses are in very good agreement with the applied stress in the longitudinal direction and is almost 0 in the transverse direction, validating the estimated level of stress in each phase. The same comparison is carried out in Figure 16 for specimens TRIP1 and B. In these cases, the equilibrium is not verified anymore since the progressive appearance of the martensite due to the TRIP effect is not taken into account. The difference between the first bisector and the calculated stress level reflects the strengthening due to the martensite formation.

Deleted: stress

Deleted: corresponds perfectly to

[Insert Figure 15 about here]

[Insert Figure 16 about here]

Since the austenite transformation rate was measured (Figure 3), it is possible to estimate the evolution of the stress within the martensitic phase by using Equation 4. This result is presented in Figure 17 for specimens TRIP1 and B. After an initial divergence presumably due to the too low initial amount of martensite, a stress around 2000 MPa is observed for both specimens. This stress level is quite similar to the stress level attained in martensite in specimen DP.

[Insert Figure 17 about here]

5. Conclusion

1 The present study has allowed a comprehensive characterisation of the flow properties of several
2 multiphase steels, some of them exhibiting a TRIP effect. The crystallographic moduli, the yield
3 strength and the flow properties of ferrite, bainite, austenite and martensite were determined using
4 neutron diffraction measurements conducted *in situ* during uniaxial tensile loading. The influence of
5 the austenite carbon content on its yield strength was estimated. The validity of the measurements
6 as well as the strengthening level resulting from the TRIP effect were assessed based on mechanical
7 equilibrium. It is of the first importance to establish the flow properties of the constitutive phases of
8 composite materials before any attempt of modelling using homogenisation procedures [33].
9
10
11
12
13
14
15
16
17

18 6. Acknowledgements

19
20
21
22 P. J. Jacques and S. Godet acknowledge the Fonds National de la Recherche Scientifique
23 (Belgium). The authors are indebted to Arcelor Research for continuous support. This work was
24 partly supported by the Belgian State, Prime Minister's Office, Federal Office for Scientific,
25 Technical and Cultural Affairs within the framework of the PAI P5/08 project "From microstructure
26 towards plastic behaviour of single- and multiphase materials".
27
28
29
30
31
32
33

34 7. References

- 35
36
37 [1] W. Bleck, in *Proc. Int. Conf. on TRIP-Aided High Strength Ferrous Alloys*, edited by B.C. De
38 Cooman (GRIPS, Bad Harzburg, 2002) pp. 13-23
39
40 [2] P.J. Jacques, *Curr Opin Solid St M* **8** 259 (2004)
41
42 [3] B.C. De Cooman, , *Curr Opin Solid St M* **8** 285 (2004)
43
44 [4] P.J. Jacques, in *Thermodynamics, Microstructures and Plasticity*, edited by A. Finel, D.
45 Mazière, M. Veron (Kluwer Academic Publishers, Dordrecht, 2002), pp. 241-250
46
47 [5] J.R. Patel, M. Cohen, *Acta Metall.* **1** 531 (1953)
48
49
50
51
52
53
54
55
56
57
58
59
60

- 1 [6] T. Angel, J. Iron and Steel Inst. 165 (1954)
- 2
- 3 [7] G.B. Olson, M. Cohen, in *Mechanical Properties and Phase Transformations in Engineering*
- 4 *Materials*, edited by S.C. Antolovich, R.O. Ritchie, W. W. Gerberich (Met. Soc. AIME, New
- 5 Orleans, 1986), pp. 367-390
- 6
- 7
- 8 [8] S. Godet, C. Georges, P.J. Jacques, in *Austenite Formation and Decomposition*, edited by E.B.
- 9 Damm, M. J. Merwin (ISS & TMS, Warrendale, 2003), pp. 523-536
- 10
- 11 [9] P. Jacques, Q. Furnémont, A. Mertens, F. Delannay, Phil. Mag. A **81** 1789 (2001)
- 12
- 13 [10] P.J. Jacques, J. Ladière, F. Delannay, Metall. Mater. Trans. A **32A** 2759 (2001)
- 14
- 15 [11] M.R. Daymond, C. Hartig, H. Mecking, Acta Mater. **53** 2805 (2005)
- 16
- 17 [12] M.R. Daymond, H.G. Priesmeyer, Acta Mater. **50** 1613 (2002)
- 18
- 19 [13] E.C. Oliver, M.R. Daymond, P.J. Withers, Acta Mater. **52** 1937 (2004)
- 20
- 21 [14] A. Baczmanski, C. Braham, Acta Mater. **52** 1133 (2004)
- 22
- 23 [15] D.H. Carter, M.A.M. Bourke, Acta Mater. **48** 2885 (2000)
- 24
- 25 [16] B. Clausen, T. Lorentzen, T. Leffers, Acta Mater. **46** 3087 (1998)
- 26
- 27 [17] M.R. Daymond, C.N. Tomé, M.A.M. Bourke, Acta Mater. **48** 553 (2000)
- 28
- 29 [18] J.W.L. Pang, T.M. Holden, T.E. Mason, Acta Mater. **46** 1503 (1998)
- 30
- 31 [19] P. Sittner, P. Lukas, V. Novaka, M.R. Daymond, G.M. Swallowe, Mater. Sc. Eng. A **378** 97
- 32 (2004)
- 33
- 34 [20] P. Sittner, P. Lukas, D. Neov, M.R. Daymond, V. Novak, G.M. Swallowe, Mater. Sc. Eng. A
- 35 **324** 225 (2002)
- 36
- 37 [21] Y. Tomota, H. Tokuda, Y. Adachi, M. Wakita, N. Minakawa, A. Moriai, Y. Morii, Acta Mater.
- 38 **52** 5737 (2004)
- 39
- 40 [22] S. Godet, J. C. Glez, Y. He, J. J. Jonas, P. J. Jacques, J Appl. Crystallogr. **37** 417 (2004)
- 41
- 42 [23] Q. Furnémont, The micromechanics of TRIP-assisted multiphase steels. PhD thesis, Université
- 43 catholique de Louvain (2003)
- 44
- 45 [24] J.W.L. Pang, T.M. Holden, T.E. Mason, J. Strain Anal. Eng. **33** 373 (1998)
- 46
- 47
- 48
- 49
- 50
- 51
- 52
- 53
- 54
- 55
- 56
- 57
- 58
- 59
- 60

- 1 [25] P. Van Houtte, L. De Buyser, *Acta Metall. Mater.* **41** 323 (1993), pp. 323-336
2
3 [26] Q. Furnemont, M. Kempf, P.J. Jacques, M. Goken, F. Delannay, *Mater. Sc. Eng. A* **328** 26
4
5 (2002)
6
7 [27] N. Tsuchida, Y. Tomota, *Mater. Sc. Eng. A* **285** 345 (2000)
8
9 [28] H.-Y. Yu, Z.-Q. Lin, G.-L. Chen, S.-H. Li, *Mater. Sc. Technol.* **21** 311 (2005)
10
11 [29] K.J. Irvine, D.T. Llewellyn, F.B. Pickering, *J. Iron Steel Inst.* 153 (1961)
12
13 [30] M. Cohen, *Trans. Metall. Soc. AIME* **224** 638 (1962)
14
15 [31] G. Krauss, *Metall. Mater. Trans. A* **32A** 861 (2001)
16
17 [32] H.K.D.H. Bhadeshia, *Bainite in Steels* (IOM Communications, London, 2001), pp. 285-342
18
19 [33] Q. Furnémont, F. Lani, T. Pardoën, F. Delannay, P.J. Jacques, *submitted to Acta Mater.*
20
21
22
23
24
25
26
27
28
29
30
31
32
33
34
35
36
37
38
39
40
41
42
43
44
45
46
47
48
49
50
51
52
53
54
55
56
57
58
59
60

Figure captions

Figure 1: SEM micrographs of the 4 microstructures considered in this study. They correspond to specimens DP (a), TRIP1 (b), TRIP2 (c) and B (d).

Figure 2: True stress – true strain curves (a) and incremental work hardening curves (b) of the four investigated specimens.

Figure 3: Austenite transformation rate during uniaxial tension for specimens B, TRIP1 and TRIP2.

Figure 4: $\{211\}_{\alpha}$ and $\{311\}_{\gamma}$ pole figures of specimen TRIP1 before any straining (a) and at the onset of necking (b).

Figure 5: *In situ* diffraction experimental set-up (a) and geometrical configuration of the Young and Poisson configurations used for the measurements (b).

Figure 6: Peak shape resulting from the superposition of the $\{211\}_{\alpha}$, $\{211\}_{\alpha'}$ and $\{112\}_{\alpha'}$ peaks in specimen DP and dotted curves corresponding to the deconvoluted peaks.

Figure 7: Evolution of the BCC, BCT or FCC lattice strains in the loading direction as a function of the macroscopic strain for specimens DP (a), TRIP1 (b), TRIP2 (c) and B (d).

Figure 8: Evolution of the BCC and FCC lattice strains in the transverse direction as a function of the macroscopic strain during tensile straining for specimens TRIP1 (a) and TRIP2 (b).

Figure 9: Comparison of the longitudinal stresses in BCC and FCC lattices calculated using equations (2a) or (3) as a function of the macroscopic true strain for specimens TRIP1 (a) and TRIP2 (b).

Figure 10: Transverse stresses in BCC and FCC lattices calculated using equation (2b) as a function of the macroscopic true strain for specimen TRIP2.

Figure 11: Evolution of the FCC and BCC or BCC and BCT phases as a function of the macroscopic true strain for specimens B (a) and DP (b).

Figure 12: Lattice strain – macroscopic true stress curves for specimens TRIP2 (a) and DP (b).

1 Figure 13: Comparison of the evolutions with true strain of the true stress and the BCC and FCC
2 lattice strains in the case of specimen TRIP2.

3
4 Figure 14: Evolution of the austenite yield strength as a function of its carbon content for several
5 TRIP-assisted multiphase steels.

6
7 Figure 15: Comparison of the macroscopic true stress and the stress recalculated from the lattice
8 strains by considering the mechanical equilibrium in the longitudinal and transverse
9 directions for specimens DP (a) and TRIP2 (b and c).

10
11 Figure 16: Comparison of the macroscopic true stress and the stress recalculated from the lattice
12 strains by the mechanical equilibrium for specimens TRIP1 (a) and B (b).

13
14 Figure 17: Estimated stress level of the martensite during straining of specimens TRIP1 (a) and B
15 (b).

Tables and Figures

(wt.%)	C	Mn	Si	P	S	Al
03C	0.29	1.42	1.41	0.012	0.02	0.04
04C	0.40	1.37	1.45	0.012	0.006	0.05

Table I : Chemical compositions (in wt. %) of the investigated steel grades

	V_{α} (%)	$V_{\alpha b}$ (%)	$V_{\gamma r}$ (%)	$V_{\alpha'}$ (%)	$[C]_{\gamma}$ (wt.%)
DP	50	/	/	50	/
TRIP 1	55	28	17	/	1.25
TRIP 2	55	33	12	/	1.5
B	/	77	23	/	1.35

Table II : Initial volume fractions of the constitutive phases of each specimen and carbon content of the retained austenite

	$\{211\}_{\alpha}$		$\{311\}_{\gamma}$	
	E^{hkl} (GPa)	ν^{hkl}	E^{hkl} (GPa)	ν^{hkl}
TRIP1	211	0.24	190	0.29
TRIP2	223	0.20	187	0.27
B	223	/	193	/
DP	216	/	/	/
Calculated (<i>Kröner</i>)	224	0.28	184	0.31

Table III : Measured and calculated elastic constants E^{hkl} and ν^{hkl} for the BCC and FCC phases for each specimen.

(MPa)	BCC ($\alpha + \alpha_6$)	FCC (γ)	BCT (α')
TRIP1	530	720	/
TRIP2	695	970	/
B	860	1140	/
DP	350	/	~ 2000
B*	820	830	/

Table IV : Measured yield strength of the different phases for each specimen.

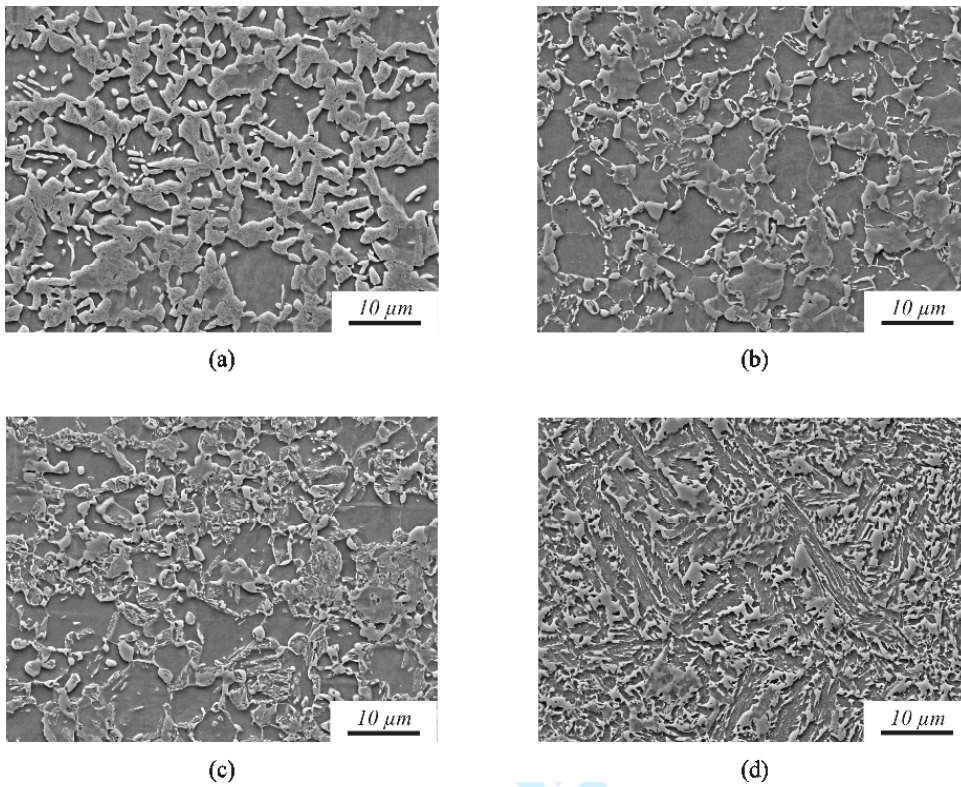


Figure 1: SEM micrographs of the 4 microstructures considered in this study. They correspond to specimens DP (a), TRIP1 (b), TRIP2 (c) and B (d).

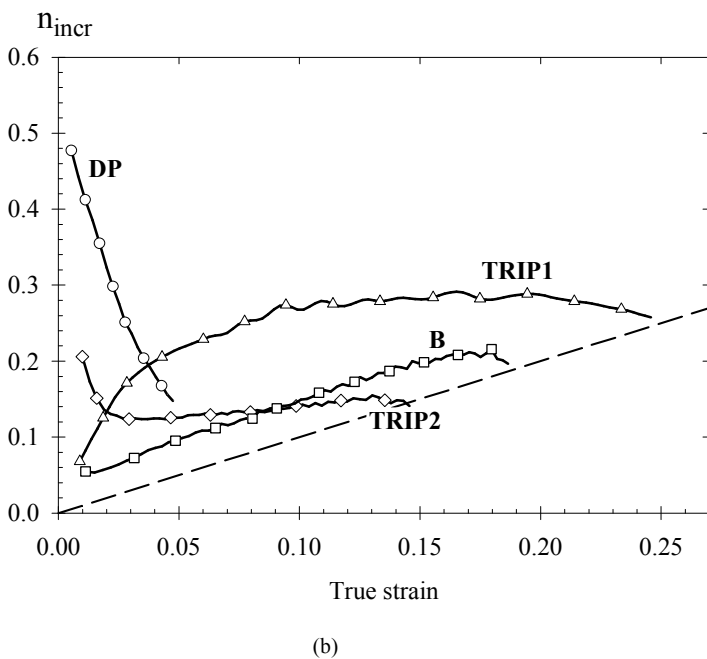
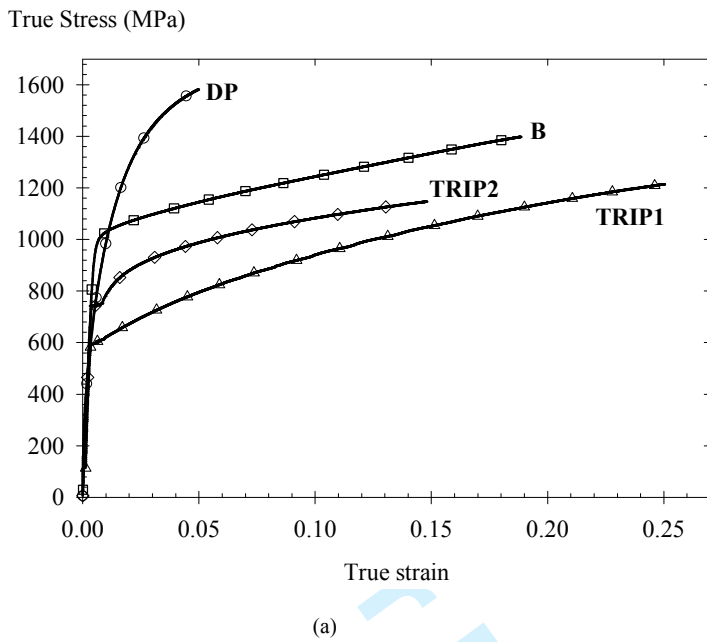


Figure 2 : True stress – true strain curves (a) and incremental work hardening curves (b) of the four investigated specimens.

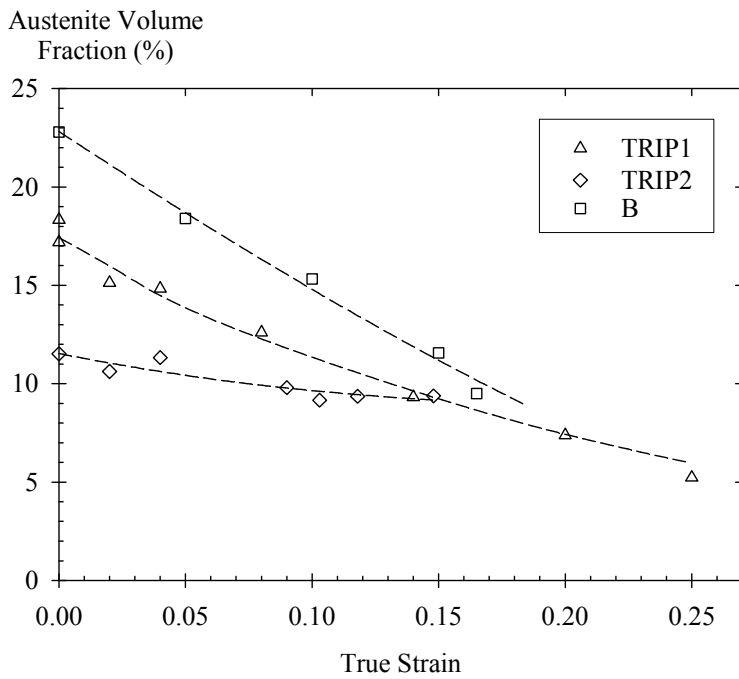


Figure 3 : Austenite transformation rate during uniaxial tension for specimens B, TRIP1 and TRIP2.

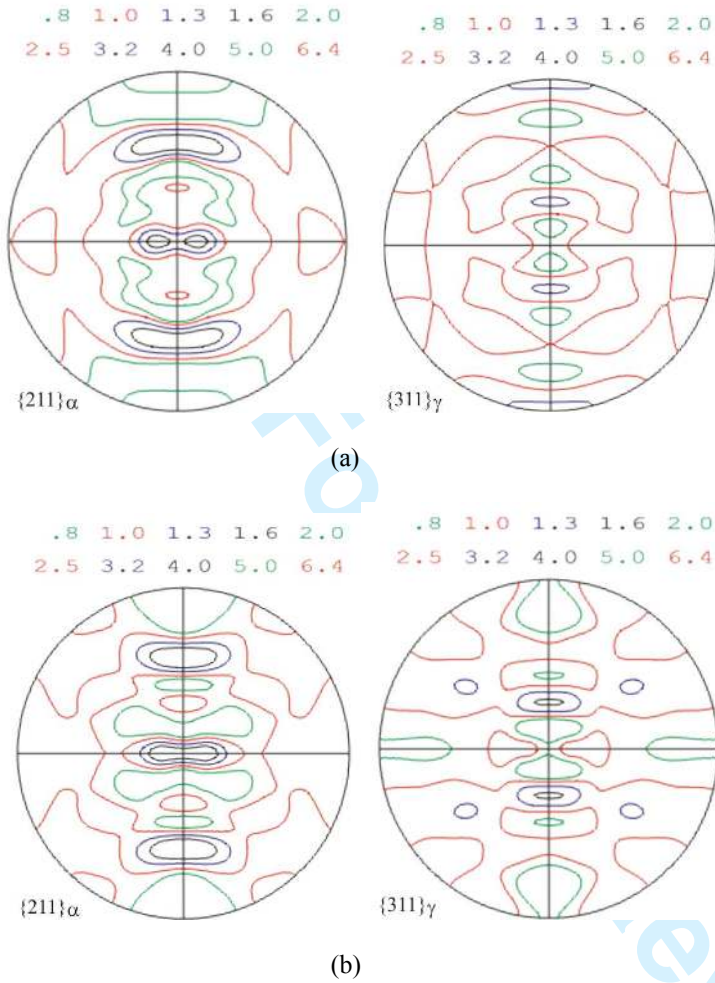
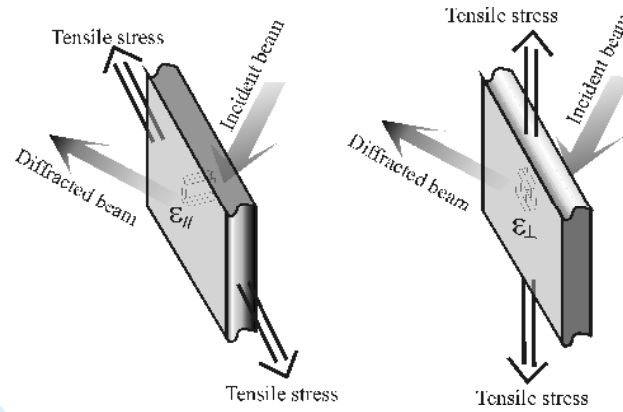
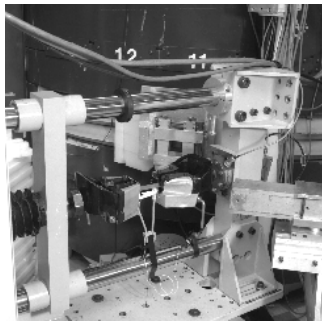


Figure 4 : $\{211\}_\alpha$ and $\{311\}_\gamma$ pole figures of specimen TRIP1 before any straining (a) and at the onset of necking (b).



33 Figure 5: *In situ* diffraction experimental set-up (a) and geometrical configuration of the Young and
34 Poisson configurations used for the measurements (b).
35
36
37
38
39
40
41
42
43
44
45
46
47
48
49
50
51
52
53
54
55
56
57
58
59
60

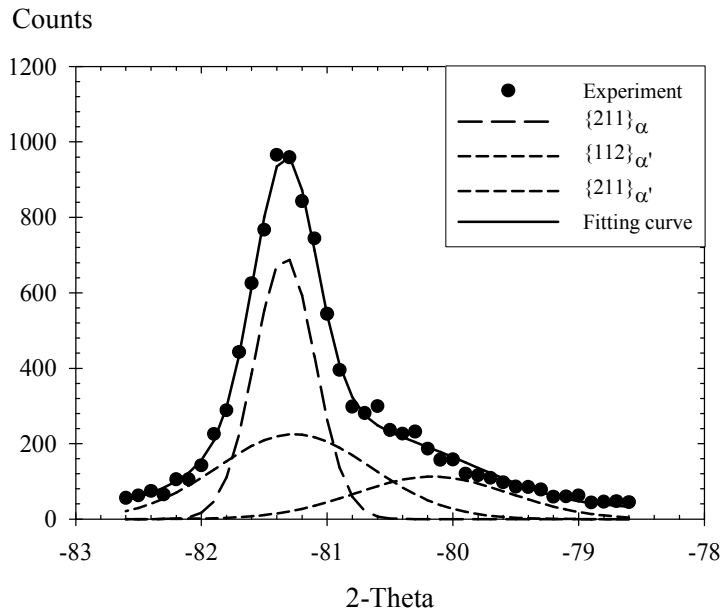


Figure 6 : Peak shape resulting from the superposition of the $\{211\}_{\alpha}$, $\{211\}_{\alpha'}$ and $\{112\}_{\alpha'}$ peaks in specimen DP and dotted curves corresponding to the deconvoluted peaks.

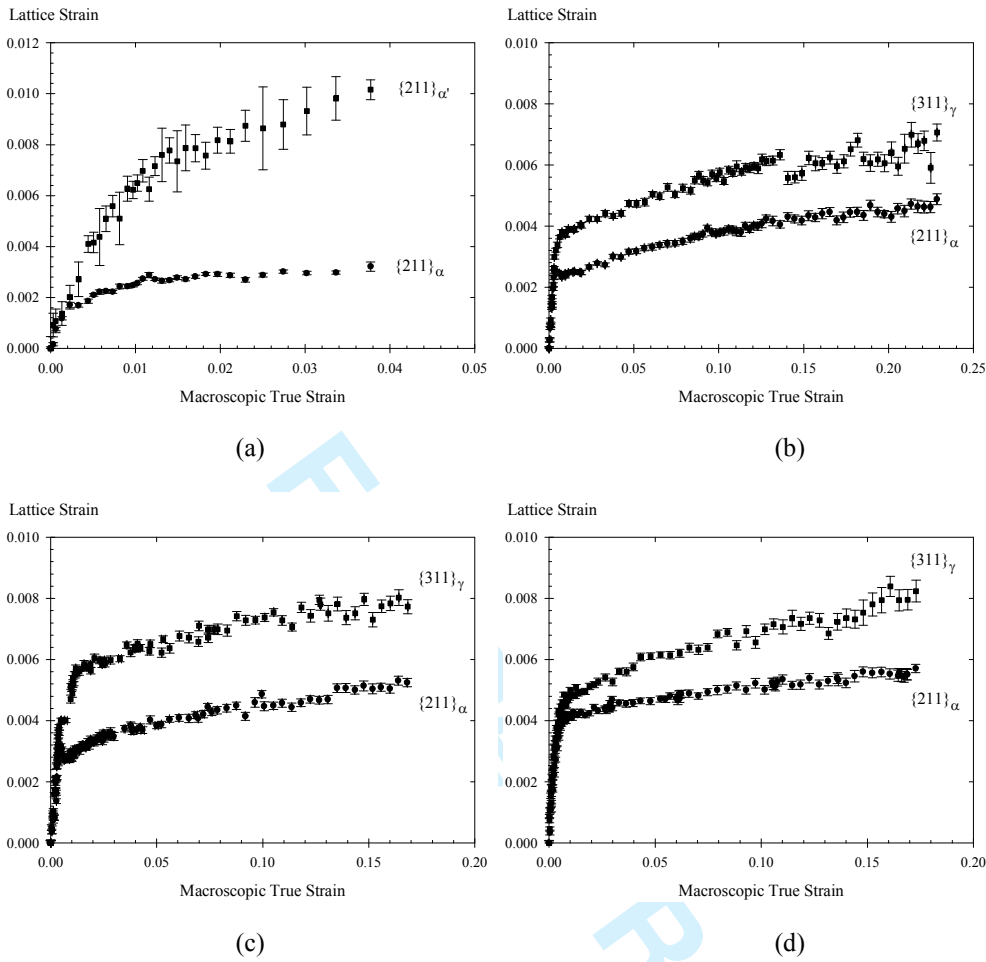
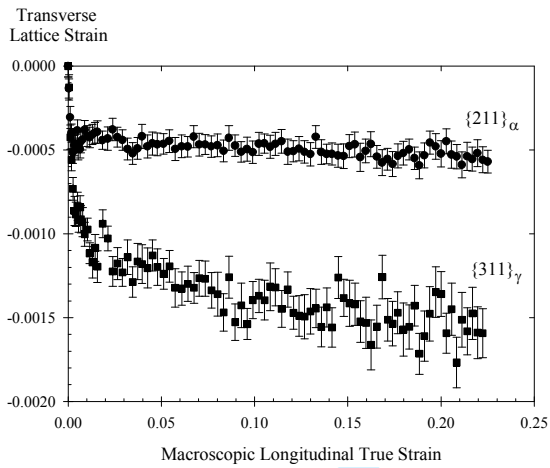
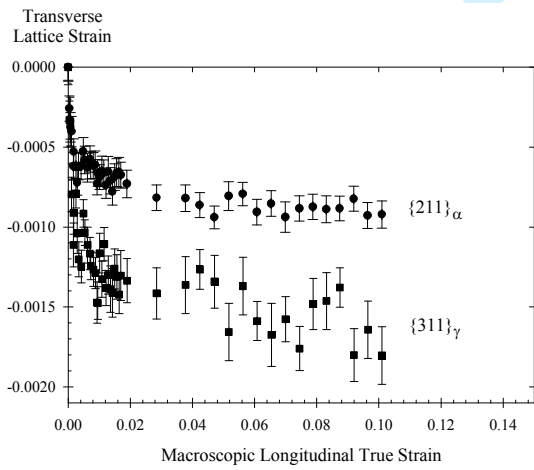


Figure 7: Evolution of the BCC, BCT or FCC lattice strains in the loading direction as a function of the macroscopic strain for specimens DP (a), TRIP1 (b), TRIP2 (c) and B (d).



(a)



(b)

Figure 8: Evolution of the BCC and FCC lattice strains in the transverse direction as a function of the macroscopic strain during tensile straining for specimens TRIP1 (a) and TRIP2 (b).

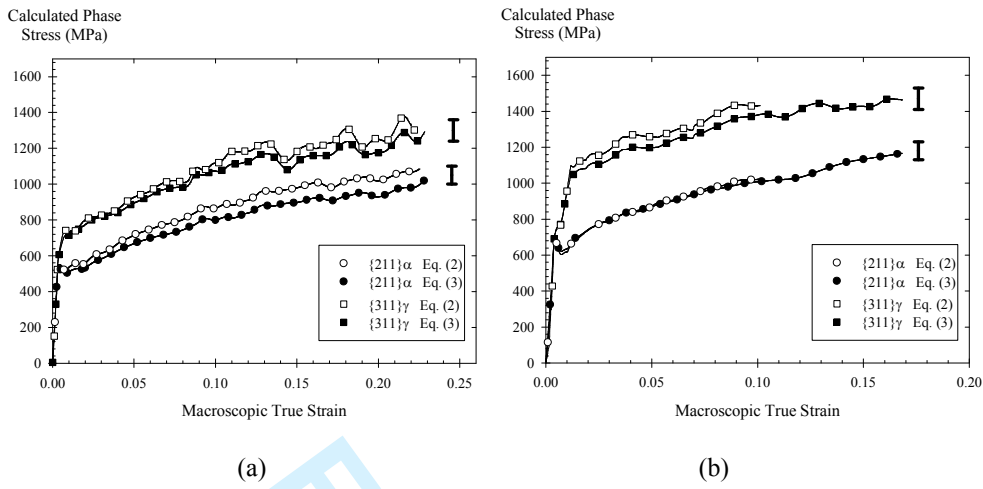


Figure 9: Comparison of the longitudinal stresses in BCC and FCC lattices calculated using equations (2a) or (3) as a function of the macroscopic true strain for specimens TRIP1 (a) and TRIP2 (b).

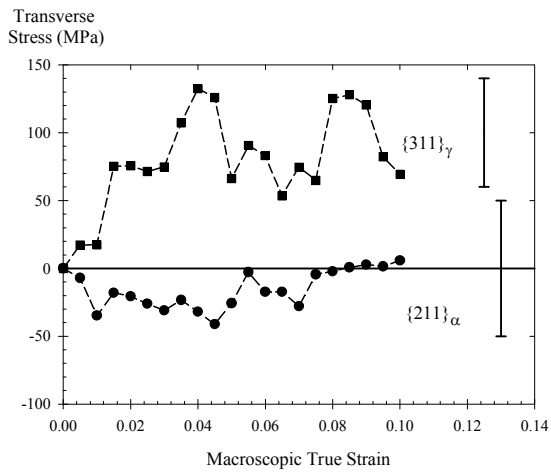


Figure 10: Transverse stresses in BCC and FCC lattices calculated using equation (2b) as a function of the macroscopic true strain for specimen TRIP2.

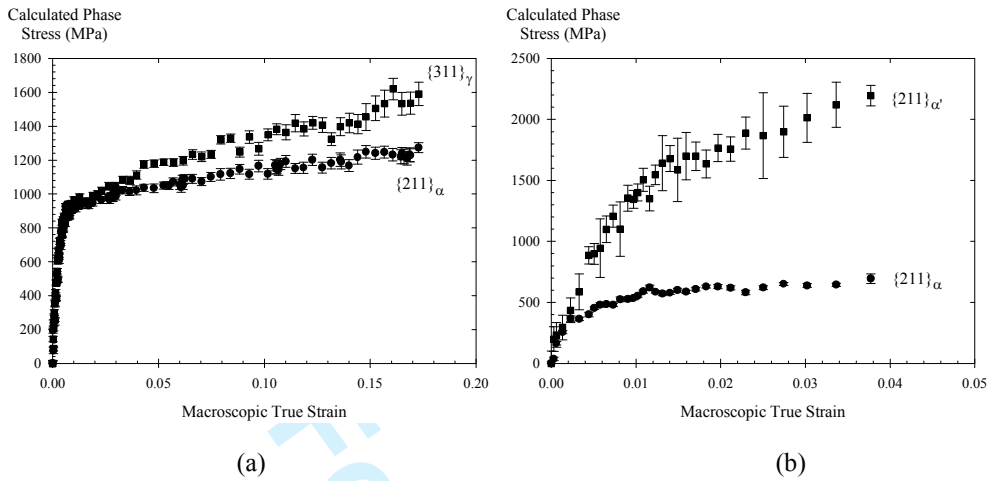
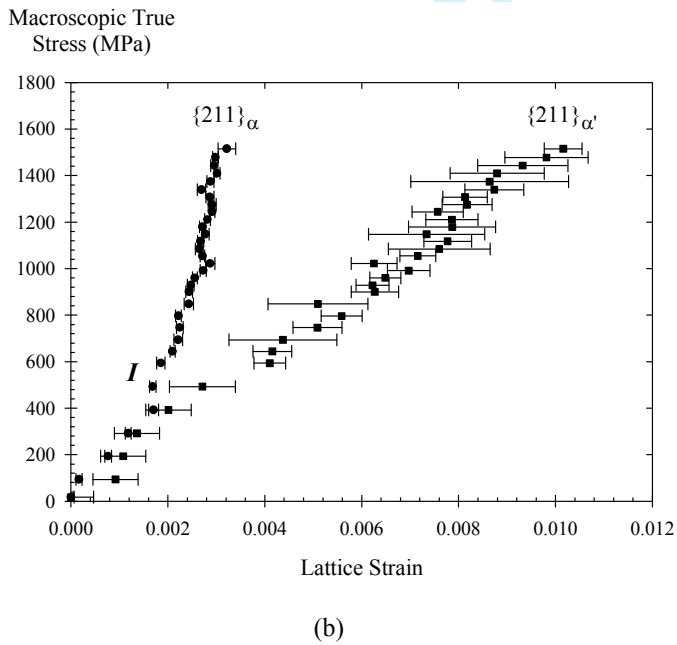
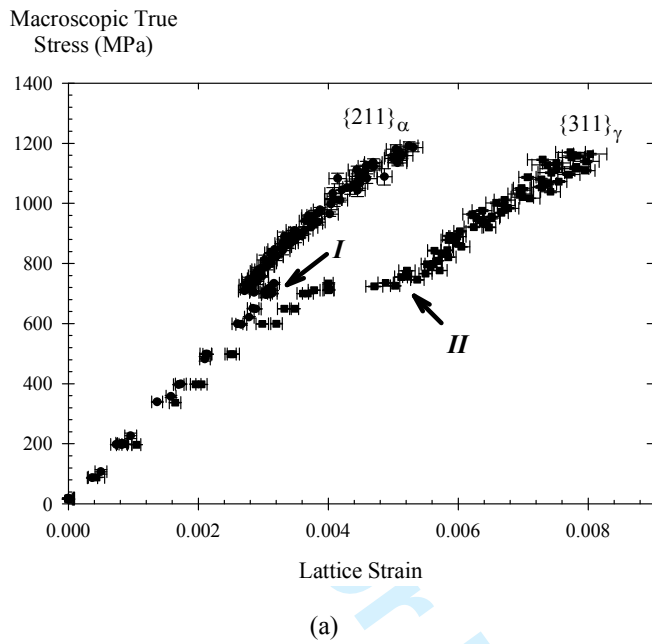


Figure 11: Evolution of the FCC and BCC or BCC and BCT phases as a function of the macroscopic true strain for specimens B (a) and DP (b).



46 Figure 12: Lattice strain – macroscopic true stress curves for specimens TRIP2 (a) and DP (b).

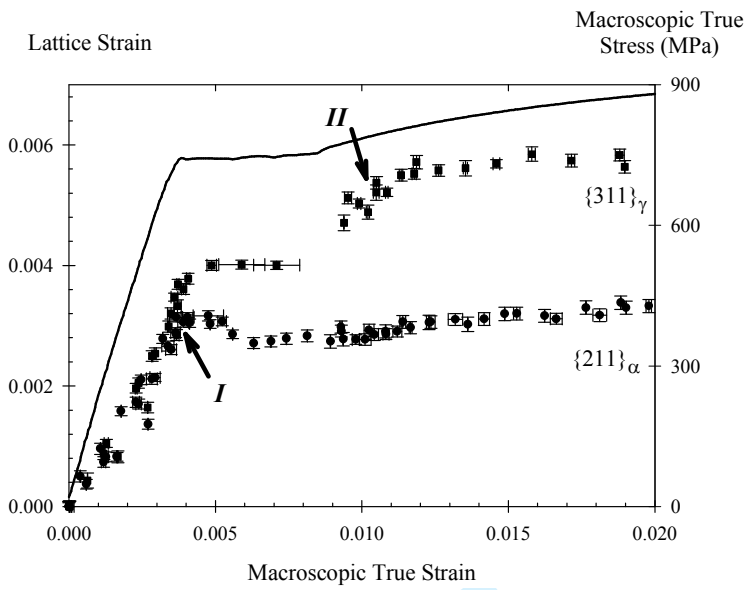


Figure 13: Comparison of the evolutions with true strain of the true stress and the BCC and FCC lattice strains in the case of specimen TRIP2.

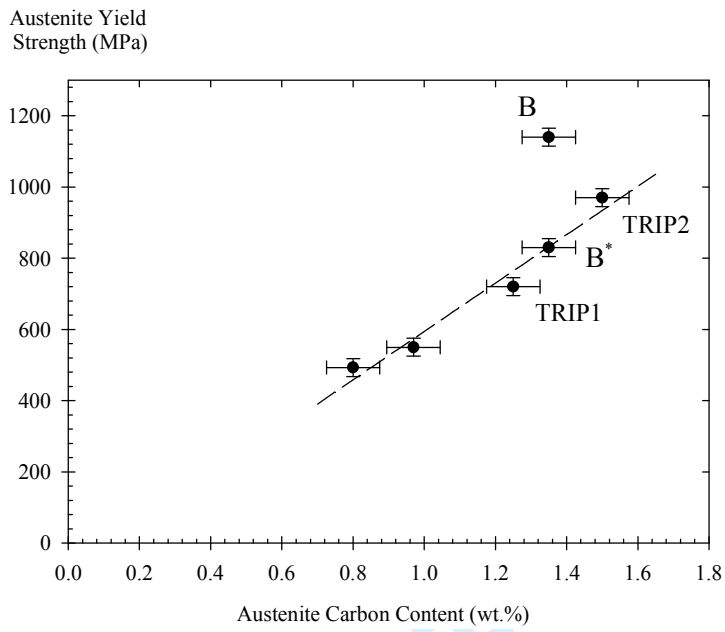


Figure 14: Evolution of the austenite yield strength as a function of its carbon content for several TRIP-assisted multiphase steels.

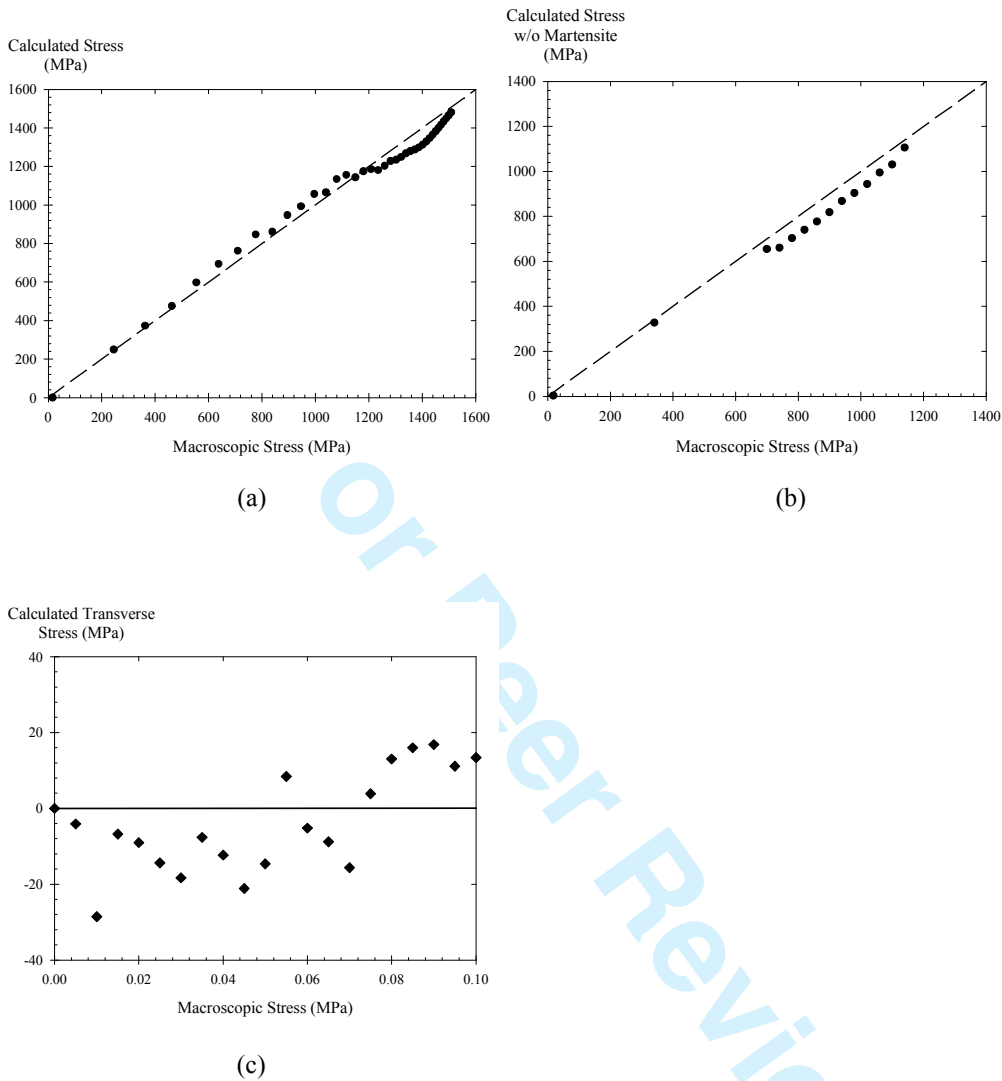


Figure 15: Comparison of the macroscopic true stress and the stress recalculated from the lattice strains by considering the mechanical equilibrium in the longitudinal and transverse directions for specimens DP (a) and TRIP2 (b and c).

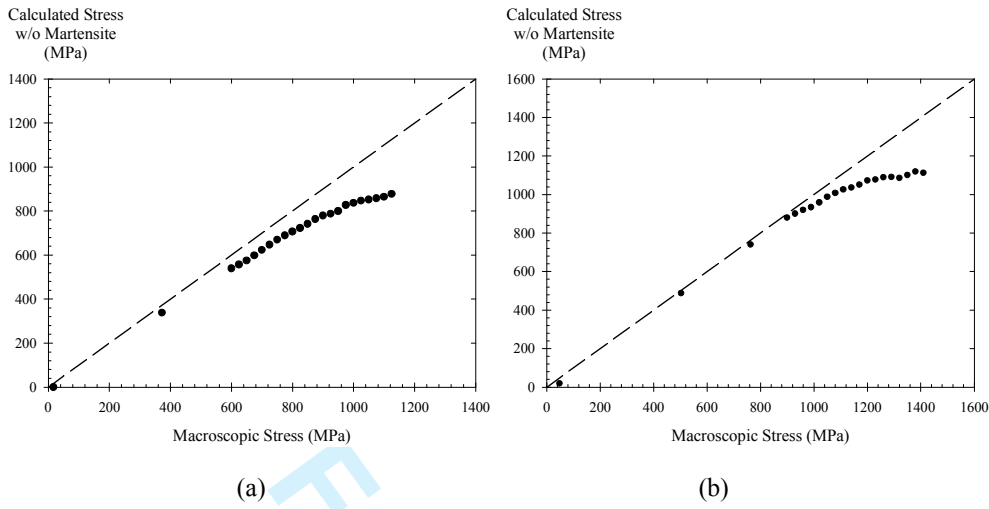


Figure 16: Comparison of the macroscopic true stress and the stress recalculated from the lattice strains by the mechanical equilibrium for specimens TRIP1 (a) and B (b).

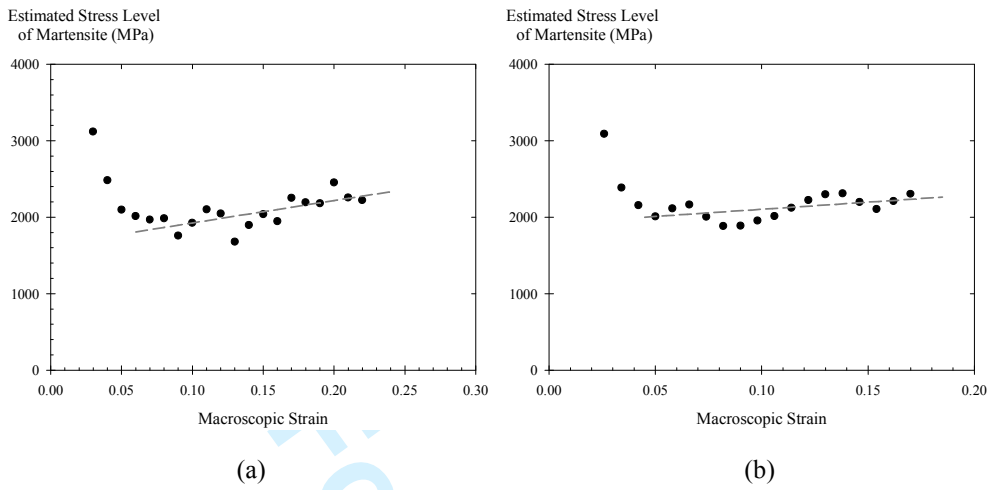


Figure 17: Estimated stress level of the martensite during straining of specimens TRIP1 (a) and B (b).